

# Cluster number counts in dark energy model with energy and momentum coupling to dark matter

C. Wongsangwal <sup>a,c</sup> K. Karwan <sup>a</sup> S. Sapa <sup>b</sup> T. Chantavat <sup>a</sup>

<sup>a</sup>The Institute for Fundamental Study, Naresuan University, Phitsanulok 65000, Thailand

<sup>b</sup>Northern College, Tak 63000, Thailand

<sup>c</sup>National Astronomical Research Institute of Thailand, Chiang Mai 50180, Thailand

E-mail: [chattreew63@nu.ac.th](mailto:chattreew63@nu.ac.th), [khampheek@nu.ac.th](mailto:khampheek@nu.ac.th), [stharporn@northern.ac.th](mailto:stharporn@northern.ac.th),  
[teeraparbc@nu.ac.th](mailto:teeraparbc@nu.ac.th)

**Abstract.** The influences on the cluster number counts from the coupling between dark energy and dark matter with momentum transfer are investigated. We find that the extrapolated linear density contrast computed from the spherical collapse model is suppressed when the strength of momentum transfer is increased. Using the Sheth-Tormen mass function, the cluster number counts are computed. The minimum mass limit in the mass integration for each redshift bin is determined by matching the predicted number counts from the  $\Lambda$ CDM model with the result from eROSITA surveys. We find that the number of clusters is maximal at a higher redshift bin, and the number of clusters in a maximum redshift bin is enhanced when the strength of momentum and energy transfers increases due to the reduction of extrapolated linear density contrast. Setting the parameters of the dark energy model with momentum coupling according to the observational constraints in [1], the predicted number counts from the coupled dark energy is larger than the result from eROSITA surveys. The statistical analysis yields a  $p$ -value of 0.189 for the proposed model relative to  $\Lambda$ CDM. Consequently, there is no statistically significant evidence of an improved fit over the standard  $\Lambda$ CDM framework based on the eROSITA cluster number counts.

---

## Contents

<b>1</b>	<b>Introduction</b>	<b>1</b>
<b>2</b>	<b>Coupled dark energy with energy and momentum transfer</b>	<b>2</b>
2.1	Coupled dark energy model	2
2.2	Scaling Lagrangian	4
2.3	Background evolution	5
2.4	Growth of linear density perturbations on small scales	7
<b>3</b>	<b>Spherical collapse</b>	<b>9</b>
<b>4</b>	<b>Cluster number counts</b>	<b>12</b>
<b>5</b>	<b>Data Analysis</b>	<b>15</b>
5.1	Sample Variance and Shot Noise Variance	15
5.2	$p$ -value estimate	17
<b>6</b>	<b>Conclusions</b>	<b>17</b>

---

## 1 Introduction

Cosmic acceleration at late time, which is strongly evidenced by numerous observations, suggests the existence of an unknown form of dark energy [2, 3]. A possible candidate for dark energy is a cosmological constant  $\Lambda$  [4]. Even though the  $\Lambda$ CDM model fits well with current observational data, it encounters a problem due to an extremely large difference between the value of the cosmological constant from theoretical predictions, and observations [5, 6]. To alleviate this problem, dark energy is supposed to be a dynamical energy component, which can be in the form of a scalar field dubbed quintessence [7–9]. Since the dynamics of quintessence are different and independent from the dynamics of radiation and matter, there is the coincidence problem, which states why the energy densities of dark energy and dark matter are of the same order at present [10–12].

Interaction between dark energy and dark matter is a possible assumption for alleviating the coincidence problem, where such coupling is expected to arise in the context of particle physics [13, 14]. Coupling between the dark sectors also arise in the frame transformation of the action for gravity. A conformal transformation leads to the interaction term  $\rho_m \dot{\phi}$  in the evolution equation for the background quintessence [15, 16], where  $\rho_m$  is the energy density of matter and  $\dot{\phi}$  is the time-derivative of the quintessence field  $\phi$ . This form of coupling generates energy transfer between the dark sectors, and has been extensively investigated in [13, 15, 17–19]. Drawbacks of this type of coupling are the following. Even though the scaling solution corresponding to matter-dominated epoch exists, it is followed by an accelerated epoch that does not satisfy observational data, i.e. the total equation of state parameter is larger than that from observations [20]. Moreover, this type of coupling leads to the enhancement of the linear growth rate of CDM perturbations [19], which makes the  $\sigma_8$  tension worse.

The  $\sigma_8$  tension is the discrepancy of the estimated  $\sigma_8$  from Cosmic Microwave Background (CMB) and that from the shear lensing analyses [21, 22]. In addition to the  $\sigma_8$  tension,  $\Lambda$ CDM model also suffers from the  $H_0$  tension between the CMB [23] and local measurements of the expansion rate of the universe [24].

Coupling between the dark sectors can also be a consequence of a momentum transfer, which is described by coupling between the field derivative  $\partial_\mu\phi$  and a CDM four velocity  $u^\mu$  in the action [25–27]. The momentum coupling can make an acceleration epoch following from the scaling epoch satisfy observational data [27]. It has been shown that the momentum coupling leads to suppression of the growth rate of CDM perturbations on small scales, which potentially solves the  $\sigma_8$  tension [28]. Observational constraints on the coupled dark energy model with energy and momentum transfer suggest that the parameter range corresponding to the absence of momentum transfer is excluded up to  $2\sigma$ , and the mean value of  $\sigma_8$  is reduced in comparison to  $\Lambda$ CDM [1].

Coupling between dark energy and dark matter can leave imprints on large-scale structure, so that we can use observational data from galaxy surveys to put constraints on couplings. Recently, results from Spectrum-Roentgen-Gamma/extended ROentgen Survey with an Imaging Array (SRG/eROSITA) all-sky survey have been released including redshift distribution of the confirmed clusters [29]. Cluster number counts from the cluster catalog in the Western Galactic Hemisphere complemented with other observational data have been used to constrain structure growth [30]. In the simplest approach, cluster number counts for given cosmological models can be estimated by supplying results from the spherical collapse model to the Press-Schechter or the Sheth-Tormen mass functions (see e.g. [31, 32]). Cluster number counts can be utilized to constrain cosmological parameters [33–35] and the power spectrum [36, 37]. Influences of the coupling between dark energy and dark matter on cluster number counts are investigated in [31, 38, 39]. The number density of galaxy clusters is investigated for various forms of the potential of dark energy in [40]. In this work, the influences of momentum coupling between the dark sectors on cluster number counts are investigated.

In Sec. 2, we present the coupled dark energy model with energy and momentum transfers considered in this work. Spherical collapse and cluster number counts are investigated in Sec. 3 and Sec. 4. The data analysis is detailed in Sec. 5, and we provide our concluding remarks in Sec. 6.

## 2 Coupled dark energy with energy and momentum transfer

### 2.1 Coupled dark energy model

We consider a dark energy model with energy and momentum coupling to cold dark matter (CDM), which can be described by the action

$$\mathcal{S} = \int d^4x \sqrt{-g} \frac{M_{\text{pl}}^2}{2} R - \int d^4x [\sqrt{-g} \rho_m(n_m) + J_m^\mu \partial_\mu \ell] + \int d^4x \sqrt{-g} L(n_c, \phi, X, Z), \quad (2.1)$$

where  $M_{\text{pl}} \equiv 1/\sqrt{8\pi G}$ , and  $R$  is the Ricci scalar. The second term in the Eq. (2.1) is the Schutz-Sorkin action describing the matter components in the form of a barotropic perfect fluid, whose dynamics are quantified by the energy density  $\rho_m$  and the particle number current  $J_m^\mu$ . The matter energy density depends on the number density  $n_m$ , while the current

is defined as

$$J_m^\mu = u_m^\mu n_m \sqrt{-g}. \quad (2.2)$$

The subscript  $m$  denotes matter components in the universe, including radiation, baryon, and CDM. The  $u_m^\mu$  is the four-velocity of the fluid. In the Schutz-Sorkin action [41],  $\ell$  is a Lagrange multiplier or Clebsch potential which is introduced to ensure the conservation of particle number. The action for a scalar field dark energy is the last term of Eq. (2.1). The kinetic term of the scalar field is expressed as  $X \equiv -g^{\mu\nu} \nabla_\mu \phi \nabla_\nu \phi / 2$ . The momentum coupling between dark energy and dark matter is encoded in  $Z \equiv u_c^\mu \nabla_\mu \phi$ , where  $u_c^\mu$  is the four velocity of CDM. The energy transfer between dark energy and dark matter arises due to the dependence of the Lagrangian for a scalar field on a number density  $n_c$  of dark matter. The Lagrangian for dark energy with the momentum and the energy coupling to dark matter can be expressed as [27]

$$L(n_c, \phi, X, Z) = -f_1(\phi, X, Z) \rho_c(n_c) + f_2(\phi, X, Z), \quad (2.3)$$

where  $\rho_c$  is the energy density of CDM,  $f_1$  and  $f_2$  are arbitrary functions that describe the energy and momentum transfer, respectively.

Varying the action (2.1) with respect to the metric tensor, we obtain the Einstein field equation

$$M_{\text{pl}}^2 G_{\mu\nu} = T_{\mu\nu}^{(r)} + (1 + f_1) T_{\mu\nu}^{(c)} + T_{\mu\nu}^{(b)} + T_{\mu\nu}^{(\phi)}, \quad (2.4)$$

where  $G_{\mu\nu}$  is the Einstein tensor and superscripts  $(r)$ ,  $(c)$ ,  $(b)$  and  $(\phi)$  denote radiation, CDM, baryon, and scalar field, respectively. The energy-momentum tensor for matter and scalar field are in the form of

$$T_{\mu\nu}^{(m)} = (\rho_m + P_m) u_\mu u_\nu + P_m g_{\mu\nu}, \quad (2.5)$$

$$T_{\mu\nu}^{(\phi)} = f_2 g_{\mu\nu} - \rho_c (f_{1,X} \nabla_\mu \phi \nabla_\nu \phi + f_{1,Z} Z u_\mu u_\nu) + f_{2,X} \nabla_\mu \phi \nabla_\nu \phi + f_{2,Z} Z u_\mu u_\nu, \quad (2.6)$$

where  $P_m$  is the pressure of the matter. The energy-momentum tensor Eq. (2.5) follows the conservation equation [27]

$$\nabla^\mu T_{\mu\nu}^{(m)} = 0, \quad (2.7)$$

while the conservation equation for the scalar field and CDM satisfies

$$(1 + f_1) \nabla^\mu T_{\mu\nu}^{(c)} + T_{\mu\nu}^{(c)} \nabla^\mu f_1 + \nabla^\mu T_{\mu\nu}^{(\phi)} = 0. \quad (2.8)$$

Multiply Eq. (2.8) by  $u_c^\nu$  and use Eq. (2.7), we obtain

$$u_c^\nu \nabla^\mu T_{\mu\nu}^{(\phi)} = -u_c^\nu \nabla^\mu \left( (1 + f_1) T_{\mu\nu}^{(c)} \right). \quad (2.9)$$

The effective energy-momentum tensor for CDM, which contains the effect of energy exchange between dark sectors, can be defined as

$$\tilde{T}_{\mu\nu}^{(c)} \equiv (1 + f_1) T_{\mu\nu}^{(c)}. \quad (2.10)$$

Due to the conservation equation  $\nabla^\mu (\tilde{T}_{\mu\nu}^{(c)} + T_{\mu\nu}^{(\phi)}) = 0$ , the left-hand-side of Eq. (2.9) can be written in terms of  $\tilde{T}_{\mu\nu}^{(c)}$ , and therefore we have

$$u_c^\nu \nabla^\mu \tilde{T}_{\mu\nu}^{(c)} = u_c^\nu T_{\mu\nu}^{(c)} \nabla^\mu f_1, \quad (2.11)$$

where we have used  $\nabla^\mu T_{\mu\nu}^{(c)} = 0$ .

## 2.2 Scaling Lagrangian

The scaling solution is an interesting feature of the dark energy for the background evolution. Before discussing the conditions for the scaling solutions, let us consider the evolution equations for the background universe. The line element of the spatially flat Friedmann-Lemaître-Robertson-Walker (FLRW) universe is given by

$$ds^2 = -dt^2 + a(t)^2 \delta_{ij} dx^i dx^j. \quad (2.12)$$

where  $\delta_{ij}$  is the Kronecker delta, and  $a(t)$  is the scale factor. The Friedmann and acceleration equations can be derived from Eq. (2.4) as

$$3M_{\text{pl}}^2 H^2 = \rho_r + \rho_b + \tilde{\rho}_c + \rho_\phi, \quad (2.13)$$

$$M_{\text{pl}}^2 (2\dot{H} + 3H^2) = -P_r - P_\phi, \quad (2.14)$$

where  $H \equiv \dot{a}/a$  is the Hubble parameter with a dot denoting derivative with respect to time.  $P_r$  and  $P_\phi$  are the pressure of the radiation and the scalar field. In this work, we set  $P_c = P_b = 0$ . From the definition Eq. (2.10), we have

$$\tilde{\rho}_c \equiv (1 + f_1) \rho_c. \quad (2.15)$$

The conservation equation (2.7) for matter components yields

$$\dot{\rho}_m + 3H(\rho_m + P_m) = 0, \quad \text{for } m = r, b, c. \quad (2.16)$$

The evolution equation for  $\tilde{\rho}_c$  is obtained from Eq. (2.11) as

$$\dot{\tilde{\rho}}_c + 3H\tilde{\rho}_c = \frac{\dot{f}_1}{1 + f_1} \tilde{\rho}_c. \quad (2.17)$$

From Eq. (2.8), we obtain

$$\dot{\rho}_\phi + 3H(\rho_\phi + P_\phi) = -\frac{\dot{f}_1}{1 + f_1} \tilde{\rho}_c. \quad (2.18)$$

The right-hand sides of Eqs. (2.17) and (2.18) correspond to the energy exchange between scalar field  $\phi$  and CDM. From Eq. (2.6), the energy density and pressure of the scalar field take the form

$$\rho_\phi \equiv -\rho_c f_{1,X} \dot{\phi}^2 - \rho_c f_{1,Z} \dot{\phi} - f_2 + f_{2,X} \dot{\phi}^2 + f_{2,Z} \dot{\phi}, \quad (2.19)$$

$$P_\phi \equiv f_2, \quad (2.20)$$

where the subscripts  $,_X$  and  $,_Z$  denote derivative with respect to  $X$  and  $Z$ , respectively. The equation of state of the scalar field is

$$w_\phi \equiv \frac{P_\phi}{\rho_\phi}. \quad (2.21)$$

We are interested in the Lagrangian for the scalar field that provides the scaling solution satisfying

$$\frac{\rho_\phi}{\tilde{\rho}_c} = \text{constant}. \quad (2.22)$$

Since the scaling solution arises due to the coupling between the scalar field and CDM, the scaling Lagrangian can be obtained by supposing that the main contribution to the dynamics of the background universe comes from the scalar field and CDM. When the scaling solution is achieved, Eq. (2.13) gives  $\rho_\phi \propto (1 + f_1)\rho_c \propto H^2$ . We suppose that  $w_\phi$  is constant during the scaling regime, so that  $P_\phi \propto \rho_\phi$  and consequently Eq. (2.20) yields  $f_2 \propto H^2$ , and each term on the left-hand side of Eq. (2.18) is proportional to  $H^3$ . Hence,  $f_1 \propto H^3(1 + f_1)/\tilde{\rho}_c \propto H(1 + f_1)$ . From these relations, the expressions for  $f_1$  and  $f_2$ , which are derived in [27], can be expressed as

$$f_1(\phi, X, Z) = e^{Q\phi/M_{\text{pl}}} g_1(Y_1, Y_2) - 1, \quad (2.23)$$

$$f_2(\phi, X, Z) = X g_2(Y_1, Y_2), \quad (2.24)$$

where  $g_1(Y_1, Y_2)$  and  $g_2(Y_1, Y_2)$  are arbitrary functions of  $Y_1$  and  $Y_2$ , which are defined as

$$Y_1 = X e^{\lambda\phi/M_{\text{pl}}}, \quad (2.25)$$

$$Y_2 = Z e^{\lambda\phi/(2M_{\text{pl}})}, \quad (2.26)$$

where  $\lambda$  is a constant parameter. Inserting Eqs. (2.23) and (2.24) into Eq. (2.3), we obtain

$$L = - \left[ e^{Q\phi/M_{\text{pl}}} g_1(Y_1, Y_2) - 1 \right] \rho_c + X g_2(Y_1, Y_2). \quad (2.27)$$

The form of  $g_1(Y_1, Y_2)$  and  $g_2(Y_1, Y_2)$  will be specified in the next section.

### 2.3 Background evolution

To study the evolution of the background universe, we define dimensionless variables as [27]

$$x \equiv \frac{\phi}{\sqrt{6} H M_{\text{pl}}}, \quad y \equiv \frac{M_{\text{pl}} e^{-\lambda\phi/(2M_{\text{pl}})}}{\sqrt{3} H}. \quad (2.28)$$

In terms of these variables,  $Y_1$  and  $Y_2$  can be expressed in the form

$$Y_1 = \frac{x^2}{y^2} M_{\text{pl}}^4, \quad Y_2 = \frac{\sqrt{2}x}{y} M_{\text{pl}}^2, \quad (2.29)$$

which gives the relation  $Y_1 = Y_2^2/2$ . To simplify the expressions for the autonomous system, we introduce

$$\epsilon_\phi \equiv \frac{\ddot{\phi}}{H\dot{\phi}}, \quad \xi \equiv \frac{\dot{H}}{H^2}. \quad (2.30)$$

The stability of the fixed points was analyzed in Ref. [27]. They found that the scaling  $\phi$ -Matter Dominated Epoch ( $\phi$ MDE) can be followed by another scaling epoch describing the cosmic acceleration. To ensure that  $g_1$  and  $g_2$  remain finite when  $y \rightarrow 0$  during  $\phi$ MDE, the functions  $g_1$  and  $g_2$  can be constructed in polynomial form as

$$g_1(Y_1, Y_2) = b_0 + \sum_{i>0} (b_i Y_1^{-i} + \tilde{b}_i Y_2^{-i}) + 2^{1-m/2} \mu \frac{Y_2^m}{Y_1^{m/2}} + \sum_{i>0, j<2i} \mu_i \frac{Y_2^j}{Y_1^i}, \quad (2.31)$$

$$g_2(Y_1, Y_2) = c_0 + \sum_{i>0} (c_i Y_1^{-i} + \tilde{c}_i Y_2^{-i}) + 2^{1-m/2} \beta \frac{Y_2^m}{Y_1^{m/2}} + \sum_{i>0, j<2i} \beta_i \frac{Y_2^j}{Y_1^i}, \quad (2.32)$$

where  $b_0, b_i, \tilde{b}_i, \mu, \mu_i, c_0, c_i, \tilde{c}_i, \beta, \beta_i$  and  $m$  are constants. In our analysis, the form of  $g_1$  is chosen such that the dark matter energy density coupled to the scalar field only through the energy coupling due to the exponential factor  $e^{Q\phi/M_{\text{pl}}}$  in Eq. (2.27). Since  $f_2$  is equal to  $P_\phi$ , the form  $g_2$  is chosen such that  $f_2$  reduces to the canonical form  $f_2 = X - V$  when the coupling disappears. Based on Eqs. (2.31) and (2.32), we choose

$$g_1(Y_1, Y_2) = 1, \quad (2.33)$$

$$g_2(Y_1, Y_2) = 1 - \frac{V_0}{Y_1} + 2^{1-m/2} \beta \frac{Y_2^m}{Y_1^{m/2}}. \quad (2.34)$$

Applying  $g_1$  and  $g_2$  to Eqs. (2.23) and (2.24), we get

$$f_1 = e^{Q\phi/M_{\text{pl}}} - 1, \quad f_2 = X - V_0 e^{-\lambda\phi/M_{\text{pl}}} + \beta (2X)^{1-m/2} Z^m. \quad (2.35)$$

Therefore, the scaling Lagrangian Eq. (2.27) can be demonstrated as

$$L = - \left( e^{Q\phi/M_{\text{pl}}} - 1 \right) \rho_c(n_c) + (X - V(\phi)) + \beta (2X)^{1-m/2} Z^m, \quad (2.36)$$

where  $V(\phi) = V_0 e^{-\lambda\phi/M_{\text{pl}}}$ ,  $\lambda$  is a constant,  $V_0$  is a positive constant,  $Q$  and  $\beta$  are constant parameters that characterize the energy and momentum exchange between CDM and scalar field, respectively.

Supplying derivatives of  $f_1$  and  $f_2$  from Eq. (2.35) to the energy-momentum tensor Eq. (2.6), we obtain the energy density and equation of state for the scalar field:

$$\rho_\phi = q_s \frac{1}{2} \dot{\phi}^2 + V_0 e^{-\lambda\phi/M_{\text{pl}}}, \quad (2.37)$$

$$w_\phi = \frac{q_s \dot{\phi}^2/2 - V_0 e^{-\lambda\phi/M_{\text{pl}}}}{q_s \dot{\phi}^2/2 + V_0 e^{-\lambda\phi/M_{\text{pl}}}}. \quad (2.38)$$

The density parameters for the scalar field and matter components are defined as

$$\Omega_\phi = q_s x^2 + \tilde{y}^2, \quad \Omega_c = \frac{\tilde{\rho}_c}{3 M_{\text{pl}}^2 H^2}, \quad \Omega_b = \frac{\rho_b}{3 M_{\text{pl}}^2 H^2}, \quad \Omega_r = \frac{\rho_r}{3 M_{\text{pl}}^2 H^2}, \quad (2.39)$$

where

$$\tilde{y} = \frac{\sqrt{V_0}}{M_{\text{pl}}}, \quad y = \sqrt{\frac{V_0}{3}} \frac{e^{-\lambda\phi/(2M_{\text{pl}})}}{M_{\text{pl}} H}. \quad (2.40)$$

Differentiating Eqs. (2.28) and (2.39) with respect to  $N = \ln a$ , we obtain

$$x' = \frac{x}{2} (6q_s x^2 - 6 + 3\Omega_c + 3\Omega_b + 4\Omega_r) + \frac{\sqrt{6}}{2q_s} (\lambda \tilde{y}^2 - Q\Omega_c), \quad (2.41)$$

$$\tilde{y}' = -\tilde{y} (6q_s x^2 - \sqrt{6} \lambda x + 3\Omega_c + 3\Omega_b + 4\Omega_r), \quad (2.42)$$

$$\Omega_b' = \Omega_b (6q_s x^2 - 3 + 3\Omega_c + 3\Omega_b + 4\Omega_r), \quad (2.43)$$

$$\Omega_r' = \Omega_r (6q_s x^2 - 4 + 3\Omega_c + 3\Omega_b + 4\Omega_r), \quad (2.44)$$

where a prime denotes derivative with respect to  $N \equiv \ln a$ . Using Eqs. (2.13), (2.14) and (2.18),  $\epsilon_\phi$  and  $\zeta$  can be written as

$$\epsilon_\phi = -3 + \frac{\sqrt{6}}{2q_s x} (\lambda y^2 - Q\Omega_c), \quad (2.45)$$

$$\zeta = -3q_s x^2 - \frac{3}{2}\Omega_c - \frac{3}{2}\Omega_b - \frac{3}{2}\Omega_r. \quad (2.46)$$

For the choice of  $f_1$  from Eq. (2.35), Eq. (2.17) becomes

$$\dot{\tilde{\rho}}_c + 3H\tilde{\rho}_c = \frac{Q}{M_{\text{pl}}} \tilde{\rho}_c \dot{\phi}, \quad (2.47)$$

and the scalar field evolves according to the equation of motion,

$$\ddot{\phi} = -3H\dot{\phi} + \frac{1}{q_s M_{\text{pl}}} \left( \lambda V_0 e^{-\lambda\phi/M_{\text{pl}}} - Q\tilde{\rho}_c \right). \quad (2.48)$$

Since in this work, we are interested in the influences of coupled dark energy on the cluster number counts, we investigate the dynamics of the universe after the onset of matter domination, so that the contributions from radiation will be ignored.

## 2.4 Growth of linear density perturbations on small scales

In this section, we present the evolution equations of linear scalar perturbation for the coupled dark energy model, where the Lagrangian is shown in Eq. (2.27). The line element for the perturbed spacetime is

$$ds^2 = -(1 - 2\Phi) dt^2 + a^2 (1 + 2\Phi) \delta_{ij} dx^i dx^j, \quad (2.49)$$

where  $\Phi$  is the metric perturbations in the Newtonian gauge, and the anisotropic perturbation is supposed to vanish. The perturbation equations can be written in terms of the following dimensionless variables

$$\delta_c = \frac{\delta\rho_c}{\rho_c}, \quad \delta_b = \frac{\delta\rho_b}{\rho_b}, \quad V_c = H v_c, \quad V_b = H v_b, \quad (2.50)$$

$$\delta\phi = \frac{H}{\dot{\phi}} \delta\phi, \quad \mathcal{K} = \frac{k}{aH}, \quad (2.51)$$

where  $\delta_c$ ,  $\delta_b$ ,  $v_c$ , and  $v_b$  are the density contrast and scalar velocity potential of CDM and baryon, respectively, and  $k$  is the comoving wavenumber. The scalar potential velocity  $v_m$  relates to spatial components of four velocity as  $u_{mi} = -\partial_i v_m$  where  $m = b, c$  and the index  $i$  refers to spatial components. Using the metric perturbation in Eq. (2.49), the Einstein equation (2.4) and the conservation equations (2.7) and (2.8) provide a set of equations for



the linear perturbations [27]:

$$6q_s x^2 \delta\varphi' - 6\Phi' + 6(1 - q_s x^2)(\xi\delta\varphi + \Phi) - 2\mathcal{K}^2\Phi + 9(\Omega_c + \Omega_b)\delta\varphi \quad (2.52)$$

$$+ 3(\Omega_c\delta_c + \Omega_b\delta_b) = 0, \quad (2.53)$$

$$\Phi' - \Phi - \xi\delta\varphi + \frac{3}{2}(\Omega_c + 2m\beta x^2)(V_c - \delta\varphi) + \frac{3}{2}\Omega_b(V_b - \delta\varphi) = 0, \quad (2.54)$$

$$\delta_c' + (\mathcal{K}^2 V_c + 3\Phi') = 0, \quad (2.55)$$

$$\delta_b' + (\mathcal{K}^2 V_b + 3\Phi') = 0, \quad (2.56)$$

$$(\Omega_c + 2m\beta x^2)V_c' - \left[\xi(\Omega_c + 2m\beta x^2) - 2m\beta x^2(3 + 2\epsilon_\phi) - \sqrt{6}Qx\Omega_c\right]V_c - \Omega_c\Psi \\ - 2m\beta x^2\delta\varphi' + \left[2m\beta x(\xi - 3 - 2\epsilon_\phi) - \sqrt{6}Q\Omega_c\right]x\delta\varphi = 0, \quad (2.57)$$

$$V_b' - (\xi + 3c_b^2)V_b - \Phi - \frac{c_b^2}{1 + w_b}\delta_b = 0, \quad (2.58)$$

$$\delta\varphi'' + (3 - \xi + 2\epsilon_\phi)\delta\varphi' + \left[\hat{c}_s^2\mathcal{K}^2 - \xi' - 3\xi + \epsilon_\phi' + \epsilon_\phi^2 + (3 - \xi)\epsilon_\phi + \frac{3}{q_s}(\lambda^2\tilde{y}^2 + Q^2\Omega_c)\right]\delta\varphi \\ + 3\hat{c}_s^2\Phi' - \Phi' - 2(3 + \epsilon_\phi)\Phi - \frac{m\beta}{q_s}\delta_c' + \frac{\sqrt{6}Q\Omega_c}{2q_s x}\delta_c = 0, \quad (2.59)$$

where

$$\hat{c}_s^2 = 1 - \frac{m\beta}{q_s}. \quad (2.60)$$

In this work, we are interested in the perturbations on small scales where the time derivative of perturbed variables can be neglected compared with their spatial derivative under the quasi-static approximation [19]. Differentiating Eqs. (2.55) and (2.56) with respect to  $N$ , eliminating the velocity perturbation using Eqs. (2.57) and (2.58), the evolution equations for the density contrast of CDM and baryons on small scales can be obtained as [27]

$$\delta_c'' + \nu\delta_c' - \frac{3}{2}(G_{cc}\Omega_c\delta_c + G_{cb}\Omega_b\delta_b) \simeq 0, \quad (2.61)$$

$$\delta_b'' + (2 + \xi)\delta_b' - \frac{3}{2}(G_{bc}\Omega_c\delta_c + G_{bb}\Omega_b\delta_b) \simeq 0, \quad (2.62)$$

where

$$\nu = \frac{2m\beta(1 + 2\beta)(5 + \xi + 2\epsilon_\phi)x^2 + (2 + \xi + \sqrt{6}Qx)[1 + (2 - m)\beta]\Omega_c}{2m\beta(1 + 2\beta)x^2 + \Omega_c[1 + (2 - m)\beta]}, \quad (2.63)$$

and

$$G_{cc} = \frac{1 + r_1}{1 + r_2}G, \quad G_{cb} = \frac{1}{1 + r_2}G, \quad (2.64)$$

$$G_{bc} = G_{bb} = G, \quad (2.65)$$

with

$$r_1 = \frac{2Q[3Q\Omega_c + \sqrt{6}m\beta x(2 + \epsilon_\phi + \sqrt{6}Qx)]}{3\Omega_c[1 + (2 - m)\beta]}, \quad (2.66)$$

$$r_2 = \frac{2m\beta(1 + 2\beta)x^2}{\Omega_c[1 + (2 - m)\beta]}. \quad (2.67)$$

The effective gravitational constant  $G_{cc}$  relevant to the growth of CDM perturbations can be larger or smaller than  $G$  depending on the parameters of the models.

### 3 Spherical collapse

Even though baryon and CDM in the coupled dark energy model collapse at different rates due to the coupling between dark energy and CDM, we simplify our investigation by treating baryon and CDM as a single fluid coupled to dark energy in the spherical collapse. The evolution equation for the density contrast can be obtained by expanding the component  $\nu = 0$  of Eq. (2.7) up to the second order as

$$\dot{\delta}_m + (1 + \delta_m)u_{,i}^i + \delta_{m,i}u^i = 0, \quad (3.1)$$

where subscript  $,i$  denotes the derivative with respect to spatial comoving coordinate  $x^i$ , and  $u^i$  is velocity of cold dark matter. Expanding the component  $\nu = i$  of Eq. (2.8) up to the second order in perturbations, we get

$$\begin{aligned} & \left(1 + \delta_m + \frac{2\beta mx^2}{\Omega_m}\right) \dot{u}_i + \frac{H[\Omega_m(2q_s - 2\sqrt{6}\beta m Qx + \sqrt{6}Qq_s x) + 2\beta mx(\sqrt{6}\lambda y^2 - q_s x)]}{q_s \Omega_m} u_i \\ & + (\dot{\delta}_m + \delta_m H(2 + \sqrt{6}Qx) + u_{,j}^j) u_i + u_{i,j} u^j - \frac{(1 + \delta_m)}{a^2} \Phi_{,i} \\ & + \frac{\sqrt{6}\beta m q_s x}{3q_s a^2 H \Omega_m} \delta \dot{\phi}_{,i} + \frac{Q\Omega_m(1 + \beta(2 - m)) + \lambda(q_s - 1 - \beta(2 - m))y^2}{q_s a^2 \Omega_m} \delta \phi_{,i} = 0. \end{aligned} \quad (3.2)$$

Inserting  $\dot{\delta}_m$  from Eq. (3.1) into Eq. (3.2), we get

$$\begin{aligned} & \dot{u}_i + \frac{H[q_s \Omega_m(1 + \delta_m)(2 + \sqrt{6}Qx) + 2\beta mx(\sqrt{6}\lambda y^2 - \sqrt{6}Q\Omega_m - q_s x)]}{q_s(\Omega_m(1 + \delta_m) + 2\beta mx^2)} u_i \\ & - \frac{\Omega_m(\delta_m u_i u_{,j}^j + u_i u_j \delta_m^j - u_{i,j} u^j)}{\Omega_m(1 + \delta_m) + 2\beta mx^2} - \frac{\Omega_m(1 + \delta_m)}{a^2[\Omega_m(1 + \delta_m) + 2\beta mx^2]} \Phi_{,i} \\ & + \frac{\sqrt{6}\beta mx}{3a^2 H[\Omega_m(1 + \delta_m) + 2\beta mx^2]} \delta \dot{\phi}_{,i} \\ & + \frac{Q\Omega_m[1 + \beta(2 - m)] + \lambda[q_s - 1 + \beta(m - 2)]y^2}{q_s a^2[\Omega_m(1 + \delta_m) + 2\beta mx^2]} \delta \phi_{,i} = 0. \end{aligned} \quad (3.3)$$

Differentiating Eq. (3.1) with respect to time, we obtain

$$\begin{aligned} & \ddot{\delta}_m + \frac{H(q_s \Omega_m(2 + \sqrt{6}Qx) - 2\beta m q_s x^2 + 2\sqrt{6}\beta mx(\lambda y^2 - Q\Omega_m))}{q_s(\Omega_m + 2\beta mx^2)} \dot{\delta}_m - \frac{\dot{\delta}_m^2}{1 + \delta_m} \\ & + \frac{(\lambda(1 + \beta(2 - m) + q_s)y^2 - (1 + \beta(2 - m))Q\Omega_m)(1 + \delta_m)\delta \phi_{,i}^i}{q_s a^2(\Omega_m + 2\beta mx^2)} \\ & - \frac{\sqrt{2}\beta m(1 + \delta_m)x\delta \phi_{,i}^i}{\sqrt{3}a^2 H(\Omega_m + 2\beta mx^2)} + \frac{(1 + \delta_m)\Omega_m \Phi_{,i}^i}{a^2(\Omega_m + 2\beta mx^2)} - \frac{\Omega_m(u^i u_{,ji}^j + u_{,ji} u^{j,i})(1 + \delta_m)}{\Omega_m + 2\beta mx^2} = 0, \end{aligned} \quad (3.4)$$

where  $\dot{u}_{,i}^i$  is eliminated using Eq. (3.3), while  $u_{,i}^i$  is eliminated using the relation  $u_{,i}^i = -\dot{\delta}_m/(1 + \delta_m)$  from Eq. (3.1). We also used a top-hat assumption  $\delta_{m,i} = 0$ . Using the identity

$$u^i \partial_i \partial_j u^j = \frac{1}{3}(\partial_i u^i)^2 - \partial_i u_j \partial^i u^j, \quad (3.5)$$

Eq. (3.4) becomes

$$\begin{aligned}
\ddot{\delta}_m + & \frac{(q_s \Omega_m (2 + \sqrt{6} Qx) - 2\beta m q_s x^2 + 2\sqrt{6} \beta m x (\lambda y^2 - Q \Omega_m)) H \dot{\delta}_m}{q_s (\Omega_m + 2\beta m x^2)} \\
- & \frac{2(2\Omega_m + 3\beta m x^2) \delta_m^2}{3(1 + \delta_m)(\Omega_m + 2\beta m x^2)} \\
- & \frac{\left( (1 + \beta(2 - m)) Q \Omega_m + \lambda (q_s - 1 - \beta(2 - m)) y^2 \right) (1 + \delta_m) \delta \phi_{,i}^i}{q_s a^2 (\Omega_m + 2\beta m x^2)} \\
- & \frac{\sqrt{2} \beta m x (1 + \delta_m) \delta \phi_{,i}^i}{\sqrt{3} a^2 H (\Omega_m + 2\beta m x^2)} + \frac{\Omega_m (1 + \delta_m) \Phi_{,i}^i}{a^2 (\Omega_m + 2\beta m x^2)} = 0.
\end{aligned} \tag{3.6}$$

On the small scales, Eq. (2.59) gives

$$\delta \phi_{,i}^i = - \frac{a^2 H^2}{2c_s^2 q_s x} \left( \sqrt{6} Q \Omega_m \delta_m - 2\beta m x \dot{\delta}_m \right), \tag{3.7}$$

and Eq. (2.53) yields

$$\Phi_{,i}^i = \frac{3}{2} a^2 H^2 \Omega_m \delta_m. \tag{3.8}$$

Inserting Eqs. (2.45), (2.46), (3.7), (3.8), and the time derivative of Eq. (3.7) into Eq. (3.6), we obtain

$$\delta_m'' + \nu \delta_m' + \mu_1 \frac{\delta_m^2}{1 + \delta_m} - \frac{3}{2} G_{cc} \Omega_m \delta_m (1 + \delta_m) = 0, \tag{3.9}$$

where we have changed the time derivative to derivative with respect to  $N$ . The coefficients  $\nu$  and  $G_{cc}$  are defined in Eq. (2.63) and (2.64). The coefficient  $\mu_1$  is

$$\mu_1 = \frac{(4 - \beta(-8 + m)) \Omega_m + 6\beta(1 + 2\beta) m x^2}{3(-1 + \beta(-2 + m)) \Omega_m - 6\beta(1 + 2\beta) m x^2}. \tag{3.10}$$

Keeping only the linear term, Eq. (3.9) reduces to Eq. (2.61) with  $\Omega_b = 0$ .

In the numerical integration, the initial condition for the density contrast can be specified by considering its behavior during the matter-dominated epoch. During this epoch, the density contrast is small, therefore the non-linear term can be neglected. Eq. (3.9) then reduces to

$$\delta_m'' + \frac{1}{2} \delta_m' - \frac{3 + 6\beta + 6Q^2}{2 + 4\beta} = 0. \tag{3.11}$$

The solution of Eq. (3.11) is

$$\delta_m = C_1 e^{-rN} + C_2 e^{rN}, \tag{3.12}$$

where  $C_1$  and  $C_2$  are the integration constant. We choose the growing solution by setting  $C_1 = 0$  and  $C_2 = \delta_i$  with

$$r = \frac{1}{4} \left[ -1 + \sqrt{1 + \frac{24}{(1 + 2\beta)} (1 + 2\beta + 2Q^2)} \right]. \tag{3.13}$$

Hence the initial conditions for Eq. (3.9) during matter-dominated epoch can be written as

$$\delta_m|_{t=t_i} = \delta_i, \quad \delta_m'|_{t=t_i} = r \delta_i, \tag{3.14}$$

where  $t_i$  is an initial time. We now consider the linear growth factor which defined as

$$D(z) \equiv \frac{\delta_m(z)}{\delta_m(z=0)}, \quad (3.15)$$

where  $\delta_m(z)$  is a linear density contrast that can be calculated from Eq. (3.11) by using the initial condition Eq. (3.14). In Table 1, we show values of parameters for each model, where the value of those parameters,  $\lambda$ ,  $Q$ ,  $\beta$ , and  $m$  are constrained by the data sets from the Planck 2018, the Phantheon supernovae, the 1-st year DES results, which are investigated in [1]. Since our focus is on the impact of momentum coupling, the parameters  $\lambda$ ,  $Q$ , and  $m$  are set to be identical across all models and equal to the mean value in [1], while strength of the momentum transfer  $\beta$  is varied. The value of  $\beta$  in the model A takes a mean value, while the models B and C take values at  $1\sigma$  and  $2\sigma$  CL, respectively.

Parameter \ Model	A	B	C
$\lambda$	0.4042	0.4042	0.4042
$Q$	-0.0312	-0.0312	-0.0312
$\beta$	0.332	0.095	0.011
$m$	2	2	2

**Table 1:** Table shows values of parameters  $\lambda$ ,  $Q$ ,  $\beta$  and  $m$  for each model.

In Fig. 1, we plot the difference ratio  $\Delta_{D(z)} \equiv (D(z)/D(z)_\Lambda) - 1$  for models A, B and C, where  $D(z)_\Lambda$  is the linear growth factor for  $\Lambda$ CDM model. The difference ratio  $\Delta_{D(z)}$  is gradually increases during  $z < 100$  and reaches the highest point at  $z \approx 0.3$  for all coupled models. However, for  $z < 0.3$ ,  $\Delta_{D(z)}$  decreases towards unity at present. The difference ratio  $\Delta_{D(z)}$  for model A is positive for the entire history of the universe, while models B and C are positive at  $z < 30$  and  $z < 10$ , respectively. The positivity of the difference ratio implies that the growth of perturbation is lower than the  $\Lambda$ CDM model because the growth factor is set to unity at present. One of the important results from the spherical collapse model is the

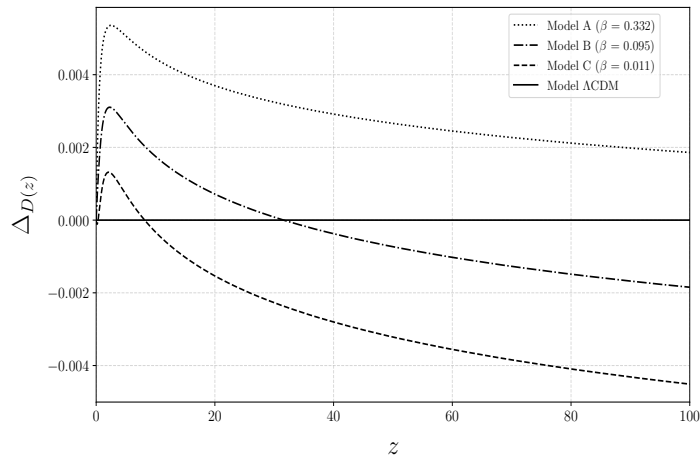


**Figure 1:** Plot of difference ratio  $\Delta_{D(z)}$ . The lines A, B, and C represent the different ratios of the models A, B, and C with the  $\Lambda$ CDM model.

extrapolated linear density contrast  $\delta_{\text{crit}}$ , which is a parameter using for calculation of the mass function. This quantity is computed by numerically solving Eq. (3.9) and searching for the initial conditions for  $\delta_m$  that leads to the collapse of overdense region, i.e.  $\delta_m \rightarrow \infty$ , at a given redshift. Supplying such initial conditions for  $\delta_m$  to Eq. (3.11), the extrapolated linear density contrast is computed by linearly evolving  $\delta_m$  to a collapsing redshift. In our calculation, we begin at the redshift that  $\delta_m$  obeys the linear evolution equation, so we can set the initial conditions for  $\delta'_m$  and  $\delta_m$  according to Eq. (3.14). Plots of  $\delta_{\text{crit}}(z)$  for models A, B, C, and  $\Lambda$ CDM are shown in Fig. 2. In the plot,  $\delta_{\text{crit}}(z)$  is suppressed when the strength of momentum coupling  $\beta$  increases, implying that momentum coupling makes overdense regions collapse more easy.

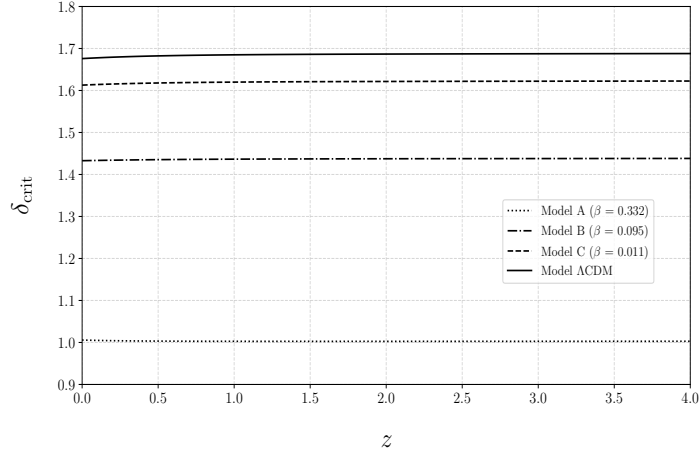


**Figure 2:** Plot of linear density contrast at collapse  $\delta_{\text{crit}}$  as a function of collapsed redshift  $z$ . The lines A, B, C, and  $\Lambda$ CDM correspond to models A, B, C, and  $\Lambda$ CDM.

#### 4 Cluster number counts

The comoving number density of collapsed objects with mass between  $M$  and  $M + dM$  can be estimated using the differential halo mass function,  $n(M, z)$ , and the extrapolated linear density contrast from the spherical collapse model by [42] as

$$n(M, z)dM = -\frac{\hat{\rho}_m}{M^2} \frac{d \ln \sigma(M, z)}{d \ln M} f(\sigma) dM, \quad (4.1)$$

where  $\hat{\rho}_m \equiv a^3 \bar{\rho}_m$  is the comoving energy density of the matter.  $\sigma(M, z)$  is the root-mean-square amplitude of linear matter variance of the region with a comoving radius  $R$  enclosing a mass  $M$  at redshift  $z$ , which can be computed from the power spectrum as [38]

$$\sigma^2(M, z) = \frac{D^2(z)}{2\pi^2} \int_0^\infty k^2 P(k, z) W^2(kR(M)) dk, \quad (4.2)$$

where  $\sigma^2(M, z) = D^2(z) \sigma^2(M, 0)$ . The comoving radius is defined as

$$R \equiv \left( \frac{3M}{4\pi\hat{\rho}_m} \right)^{1/3}, \quad (4.3)$$

which represents the radius of the background region enclosing mass  $M$ . The quantity  $P(k, z)$  denotes the linear power spectrum of the matter perturbations at redshift  $z$ , and weighted by the Fourier-transformed window function of a spherical top-hat function

$$W(kR) = \frac{3}{(kR)^3} \left( \sin(kR) - kR \cos(kR) \right), \quad (4.4)$$

which serves as a smoothing filter for the density field. The mass function  $f(\sigma)$  is defined as the fraction of mass in collapsed regions per unit interval in  $\ln \sigma^{-1}$ .

In our analysis, we use the Sheth-Tormen mass function given by [43, 44]

$$f_{\text{S-T}}(\sigma) = A \sqrt{\frac{2a}{\pi}} \left[ 1 + \left( \frac{\sigma^2}{a\delta_{\text{crit}}^2} \right)^p \right] \frac{\delta_{\text{crit}}}{\sigma} \exp \left[ -\frac{a\delta_{\text{crit}}^2}{2\sigma^2} \right], \quad (4.5)$$

where  $\delta_{\text{crit}}$  is the linear extrapolated density contrast at collapsed redshift. The parameter  $A$  is a normalization constant equal to 0.3222 for our mass limit. The values  $a = 0.707$  and  $p = 0.3$  are the values according to the best fit with  $\Lambda$ CDM model [43]. Setting  $a = 1$ , and  $p = 0$ , the Sheth-Tormen mass function reduces to the Press-Schechter mass function. The linear matter power spectrum for coupled dark energy model is computed using the modified version of CLASS, with cosmological parameters supplied according to the best-fit values in [1], while that for  $\Lambda$ CDM model is computed using the cosmological parameters according to observational constraints in [24].

Model	A	B	C	$\Lambda$ CDM
$\sigma_8$	0.802	0.808	0.811	0.811

**Table 2:** The value of  $\sigma_8$  for model parameters given by Table 2.

The number of galaxy clusters in the redshift interval  $\Delta z$  with mass larger than  $M_{\text{min}}$  can be computed by integrating Eq. (4.1) over the mass as

$$N = f_{\text{sky}} \frac{dV_e}{dz} \Delta z \int_{M_{\text{min}}}^{\infty} n(M) dM, \quad (4.6)$$

where  $f_{\text{sky}}$  is the observed sky fraction,  $dV_e/dz \equiv 4\pi r(z)^2/H(z)$  is the comoving volume element per unit redshift, and  $r(z)$  is the comoving distance at redshift  $z$ . The volume element is evaluated at the midpoint of redshift bins. To understand the influence of momentum coupling on the number counts, we first study how momentum coupling affects the comoving volume element per unit redshift  $dV_e/dz$  and  $\delta_{\text{crit}}/(\sigma_8 D(z))$  for each model. The values of  $\sigma_8$  is the root-mean-square amplitude of linear matter variance at a comoving radius of  $8 h^{-1} \text{Mpc}$  calculated at  $z = 0$ . The values of  $\sigma_8$  for all coupled models are shown in Table 2. This shows that the  $\sigma_8$  is decreased when the strength of the momentum coupling constant  $\beta$  is increased. In Fig. 3, we see that the evolution of  $dV_e/dz$  for models A, B, and C behaves rarely difference from the  $\Lambda$ CDM model for our choices of parameters.

It follows from Fig. 4 that the ratio  $\delta_{\text{crit}}/(\sigma_8 D(z))$  decreases from high redshift to the present. At particular redshift, this ratio is suppressed when  $\beta$  increases. This can be seen from Fig. 1 that a nonzero  $\beta$  weakly enhances the growth factor  $D(z)$ , while  $\delta_{\text{crit}}$  is significantly suppressed as shown in Fig. 2. Consequently, the ratio  $\delta_{\text{crit}}/(D(z)\sigma_8)$  reduces when momentum coupling  $\beta$  increases.

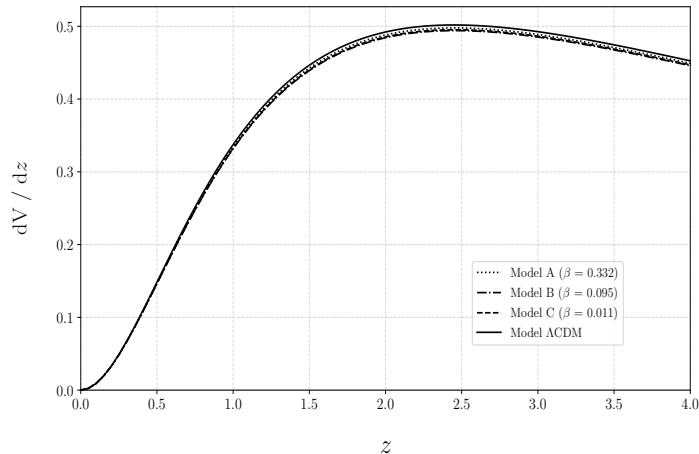


**Figure 3:** Plots of comoving volume element  $V_e$  as a function of redshift  $z$ . The lines A, B, C, and  $\Lambda$ CDM correspond to models A, B, C, and  $\Lambda$ CDM.

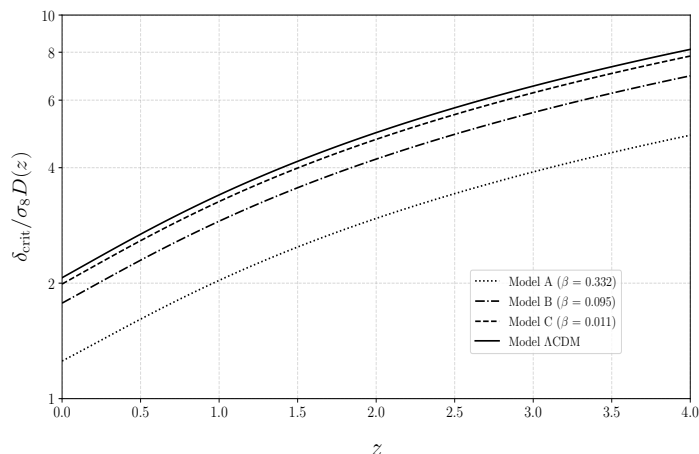


**Figure 4:** Plots of  $\delta_{\text{crit}}/(\sigma_8 D(z))$  as a function of redshift  $z$ . The lines A, B, C, and  $\Lambda$ CDM correspond to models A, B, C, and  $\Lambda$ CDM, in order.

In the calculation of cluster number counts, we set the sky coverage  $f_{\text{sky}} = 0.31$  ( $\approx 12,791 \text{ deg}^2$ ), according to the eROSITA surveys [45]. The mass limit  $M_{\text{min}}$  for each redshift bin is chosen such that the number of clusters computed from Eq. (4.6) for the  $\Lambda$ CDM model matches the results from the eROSITA surveys [45]. From Fig. 5, we observe that the number of clusters per redshift is significantly enhanced as the momentum coupling  $\beta$  increases, compared with the  $\Lambda$ CDM model. This enhancement arises from the behavior of the ratio  $\delta_{\text{crit}}/(\sigma_8 D(z))$  discussed earlier. Even though the momentum transfer leads to the suppression of the growth of density perturbations on small scales which potentially alleviated  $\sigma_8$  tension, it enhances the number of clusters per redshift intervals which may exceed the observational bound from the eROSITA surveys.

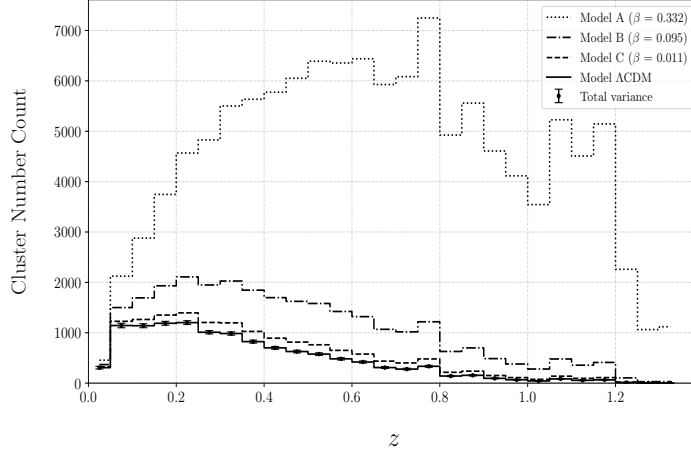


**Figure 5:** Plots of the number of clusters  $N$  per redshift bin  $\Delta z$ . The lines A, B, C, and  $\Lambda$ CDM represent the number of clusters for the models A, B, C, and  $\Lambda$ CDM. The errors in the  $\Lambda$ CDM are estimated from sample variances and shotnoise variances.

## 5 Data Analysis

### 5.1 Sample Variance and Shot Noise Variance

To calculate the uncertainties for each redshift bin, we combine the sample variance and the shot noise variance, as detailed in [46]. For a given observational volume, the sample variance ( $s_{sv}^2$ ), also known as sample covariance, represents the statistical variance of the observed signal  $X$ . We shall denote  $s$  as fractional uncertainties (i.e.  $s \equiv \Delta X/X$ ) and  $S$  as the absolute uncertainties ( $S \equiv \Delta X$ ).

For example, if we define the number density ( $n$ ) as our signal, the sample variance is expressed as:

$$s_{sv}^2 = \frac{\langle n^2 \rangle - \bar{n}^2}{\bar{n}^2} = b^2(M, z) \sigma^2(M, z). \quad (5.1)$$

Here,  $\bar{n}$  is the averaged cluster number density,  $\langle n^2 \rangle$  denotes the second moment (or the ensemble average) of  $n^2$  over the entire sample, and  $b(M, z)$  is the bias parameters [47].  $\sigma(M, z)$  is the root-mean-square amplitude of linear matter variance of the region with a comoving radius  $R$  enclosing a mass  $M$  as in Eq. (4.2). The absolute uncertainty due to sample variance is then  $S_{sv} = \bar{n} s_{sv} = \bar{n} b(M, z) \sigma(M, z)$ . In applying to cluster survey, we will implement the effective bias, which is expressed as

$$b_{\text{eff}}(z) = \frac{\int_{M_{\min}(z)}^{M_{\max}} b(M, z) n(M, z) dM}{\int_{M_{\min}(z)}^{M_{\max}} n(M, z) dM}. \quad (5.2)$$

The integral is calculated from  $M_{\min}(z)$ , which is the lower mass limit corresponding to the eROSITA cluster survey for each redshift bin. We assume the Sheth-Mo-Torman cluster bias from [48] which is expressed in as

$$b(v, z) = 1 + \frac{1}{\sqrt{a} \delta_{\text{crit}}(z)} \left[ \sqrt{a} (av^2) + \sqrt{a} b(av^2)^{1-c} - \frac{(av^2)^c}{(av^2)^c + b(1-c)(1-c/2)} \right], \quad (5.3)$$



where  $a = 0.707, b = 0.5, c = 0.6$  and  $\nu \equiv \delta_{\text{crit}}(z)/\sigma(M, z)$ . The absolute sample variance for the  $i^{\text{th}}$  redshift bin is [49]

$$S_{\text{sv},i}^2 = N_i^2 b_{\text{eff}}^2(z_i) \int \frac{d^3k}{(2\pi)^3} P(k, z_i) W_i^2(\mathbf{k}), \quad (5.4)$$

where the index  $i$  denotes the redshift bins, and all quantities correspond to these respective bins.  $N_i$  denotes the number of clusters observed in the  $i$ th bin. The window function  $W_i$  (differs from the one in Eq 4.4 which assumes the spherical top-hat) for a redshift slice of a cone,  $W_i(\mathbf{k})$  is given by [50]

$$W_i(\mathbf{k}) = \frac{4\pi}{V_i} \int_{\Delta z_i} dz \frac{dV_e}{dz} \sum_{\ell=0}^{\infty} \sum_{m=-\ell}^{\ell} (i)^\ell j_\ell [k\chi(z_i)] Y_{\ell m}(\hat{\mathbf{k}}) K_\ell, \quad (5.5)$$

where  $dV_e/dz$  is the comoving volume element and  $V_i$  is the volume of the redshift slice.  $j_\ell [kr(z)]$  are the spherical Bessel functions,  $Y_{\ell m}(\hat{\mathbf{k}})$  is the spherical harmonics.

$$Y_{\ell m}(\hat{\mathbf{k}}) = (-1)^m \sqrt{\frac{2\ell+1}{4\pi} \frac{(\ell-m)!}{(\ell+m)!}} P_\ell^m(\cos\theta) e^{im\phi}. \quad (5.6)$$

$K_\ell$  is the coefficient of the expansion in the spherical harmonics of the angular part of the window function, defined from

$$K_{\ell m} \equiv \frac{1}{\Omega_{\text{sky}}} \int d\Omega W(\hat{n}) Y_{\ell m}^*(\hat{n}). \quad (5.7)$$

Due to azimuthal symmetry, all spherical harmonic components with  $m \neq 0$  vanish, leaving only the  $m = 0$  mode non-zero;

$$K_\ell = \frac{1}{\Omega_{\text{sky}}} \int d\Omega W(\hat{n}) \sqrt{\frac{2\ell+1}{4\pi}} P_\ell(\cos\theta), \quad (5.8)$$

where  $P_\ell(\cos\theta)$  are Legendre polynomials.  $\theta_s$  is the angular extended of the survey

$$\Omega_{\text{sky}} = 2\pi (1 - \cos\theta_s) = 4\pi f_{\text{sky}}. \quad (5.9)$$

Here we use  $f_{\text{sky}} = 0.31$ , and  $\theta_s \approx 67.67^\circ$ . For full sky survey  $\Omega_{\text{sky}} = 4\pi$ . Then the  $K_\ell$  can be expressed as follows

$$\begin{aligned} K_\ell &= \frac{1}{2\sqrt{\pi}} \quad \text{for } \ell = 0, \\ K_\ell &= \sqrt{\frac{\pi}{2\ell+1}} \frac{P_{\ell-1}(\cos\theta_s) - P_{\ell+1}(\cos\theta_s)}{\Omega_{\text{sky}}} \quad \text{for } \ell \neq 0. \end{aligned} \quad (5.10)$$

The shot noise variance (or Poisson variance), denoted as  $s_{\text{sn}}^2$  (for fractional) or  $S_{\text{sn}}^2$  (for absolute), represents a fundamental type of statistical fluctuation that naturally and unavoidably occurs in systems that detect random and discrete events. It is given by:

$$s_{\text{sn}}^2 = \frac{1}{X}, \quad S_{\text{sn}}^2 = X, \quad (5.11)$$

where  $X$  is the observed signal (e.g. the number of detected clusters in the bin). In case of the cluster number count the absolute shot noise variance is

$$S_{\text{sn},i}^2 = N_i. \quad (5.12)$$

We assume that the statistical correlation between different redshift bins is negligible. Therefore, the total statistical variance for each redshift bin is the squared sum of the sample variance and shot noise variance;

$$S_{\text{total},i}^2 = S_{\text{sv},i}^2 + S_{\text{sn},i}^2. \quad (5.13)$$

## 5.2 $p$ -value estimate

Fig. 5 shows the expected number count for the  $\Lambda$ CDM model compared with the other models, including the uncertainties derived in Sec. 5.1. We use  $p$ -value estimation to quantitatively assess the consistency (or closeness) between the alternative models and our null hypothesis ( $\Lambda$ CDM in this case). We perform this assessment by computing the value of the  $\chi^2$  from our cluster number counts in Fig. 5:

$$\chi^2 = \sum_{i=1}^{N_{\text{dof}}} \frac{(N_i^X - N_i^\Lambda)^2}{S_{\text{total},i}^2}, \quad (5.14)$$

where  $N_i^X$  is the number count for bin  $i^{\text{th}}$  on model  $X$  ( $X = A, B$  or  $C$ ).  $N_i^\Lambda$  is the corresponding number count for the  $\Lambda$ CDM model, and  $S_{\text{total},i}^2$  is the absolute uncertainty for that bin in Eq. (5.13).  $N_{\text{dof}}$  is the number of degree of freedom.

The overall uncertainty was estimated by incorporating the model parameter uncertainties from [1], following the procedure described in Sec. 3. In particular, the lower bound for  $\beta$  (see Eq. (5.2) in [1]) is adopted as a  $2\sigma$  uncertainty. Accordingly, in Fig. 5, Model A represents the mean cluster count, while Model B corresponds to the  $1\sigma$  lower limits arising from the variation of model parameters. The  $1\sigma$  uncertainties for each bin are estimated using Model C, which yields larger uncertainties than Model B, thereby providing a conservative estimate. The calculated value of  $\chi^2$  is then justified using the  $\chi^2$ -distribution [51]:

$$p_\nu(x) = \frac{1}{\Gamma(\nu/2)} \left(\frac{x}{2}\right)^{\nu/2} \frac{e^{(-x/2)}}{x}, \quad (5.15)$$

where  $x$  is the computed value of  $\chi^2$  and  $\nu$  is the number of degree of freedom ( $N_{\text{dof}}$ ).  $\Gamma(x)$  is the Gamma function. The dataset comprises 27 redshift bins with 4 free parameters (see Table 1), resulting in 23 degrees of freedom. Our model yields an effective (reduced) chi-squared of  $\chi_\nu^2 = 1.06$  and a  $p$ -value of 0.189. Based on the  $\chi^2$ -distribution  $p$ -values, the  $\Lambda$ CDM model (the simpler model) is adequate for describing the observed number counts. With  $p$ -value  $> 0.05$ , there is no statistically significant evidence to suggest the more complex model (coupled dark energy and dark matter) offers a superior fit.

## 6 Conclusions

We investigate the influences of energy and momentum coupling between dark energy and dark matter on structure formation by using the spherical collapse model and the Sheth-Tormen mass function to estimate cluster number counts.

When the momentum coupling parameter  $\beta$  increases, the growth rate of matter perturbations on small scales is suppressed. Consequently, the value of  $\sigma_8$  decreases. We find that the extrapolated linear density contrast at the collapsing redshift is also suppressed as the strength of momentum coupling increases. Since the extrapolated linear density contrast is much more suppressed compared with the growth rate of matter perturbation, the magnitude of the mass function at particular redshifts is enhanced with the increasing strength of momentum coupling.

Using the Sheth-Tormen mass function, we compute cluster number counts by setting the mass limit for each redshift bin such that the number counts of each bin for  $\Lambda$ CDM matches with the result from the eROSITA surveys. We find that the predicted number of clusters per redshift interval enhances when the momentum coupling increases. Choosing the model parameters based on the observational constraint in [1], the predicted number counts from the momentum coupling model is larger than the result from the eROSITA surveys. Even though the strength of momentum coupling is set to the lower bound of  $2\sigma$  in [1], the predicted number counts from coupled dark energy model is higher than the result from the eROSITA survey. This suggests that the observational data for cluster number counts might not prefer momentum coupling between dark energy and dark matter. However, this may be a drawback of treated baryon and CDM as a single fluid in spherical collapse analysis.

Our data analysis demonstrates the calculation of the total statistical variance  $S_{\text{total},i}^2$  for each redshift bin in the  $\Lambda$ CDM model, as shown in Fig. 5. We also estimated the  $\chi^2$  values and corresponding  $p$ -values to assess the consistency between coupled model and  $\Lambda$ CDM model. The results show that the  $p$ -values for coupled model are greater than 0.05. This suggests that the coupled dark energy and dark matter model with additional parameters do not provide statistically significant evidence for an improved fit over the  $\Lambda$ CDM model based on the observed cluster number counts from eROSITA alone.

## Acknowledgement

We would like to thank Nicolas Clerc for his helpful suggestions. This work was supported by NARIT through the Scholarship for Research student, and was received funding support from the NSRF via the Program Management Unit for Human Resources & Institutional Development, Research and Innovation [grant number B37G660013].

## References

- [1] X. Liu, S. Tsujikawa and K. Ichiki, *Observational constraints on interactions between dark energy and dark matter with momentum and energy transfers*, *Phys. Rev. D* **109** (2024) 043533 [2309.13946].
- [2] L. Amendola and S. Tsujikawa, *Dark Energy: Theory and Observations*, Cambridge University Press, Cambridge (2010).
- [3] K. Bamba, S. Capozziello, S. Nojiri and S.D. Odintsov, *Dark energy cosmology: the equivalent description via different theoretical models and cosmography tests*, *Astrophys. Space Sci.* **342** (2012) 155 [1205.3421].
- [4] S.M. Carroll, *The Cosmological Constant*, *Living Reviews in Relativity* **4** (2001) 1 [astro-ph/0004075].
- [5] V. Sahni, *The cosmological constant problem and quintessence*, *Classical and Quantum Gravity* **19** (2002) 3435 [astro-ph/0202076].

- [6] S. Weinberg, *The cosmological constant problem*, *Reviews of Modern Physics* **61** (1989) 1.
- [7] B. Ratra and P.J.E. Peebles, *Cosmological consequences of a rolling homogeneous scalar field*, *Phys. Rev. D* **37** (1988) 3406.
- [8] S.M. Carroll, *Quintessence and the Rest of the World: Suppressing Long-Range Interactions*, *Phys. Rev. Lett.* **81** (1998) 3067 [[astro-ph/9806099](#)].
- [9] E.J. Copeland, M. Sami and S. Tsujikawa, *Dynamics of Dark Energy*, *International Journal of Modern Physics D* **15** (2006) 1753 [[hep-th/0603057](#)].
- [10] I. Zlatev, L. Wang and P.J. Steinhardt, *Quintessence, Cosmic Coincidence, and the Cosmological Constant*, *Phys. Rev. Lett.* **82** (1999) 896 [[astro-ph/9807002](#)].
- [11] S. Dodelson, M. Kaplinghat and E. Stewart, *Solving the Coincidence Problem: Tracking Oscillating Energy*, *Phys. Rev. Lett.* **85** (2000) 5276 [[astro-ph/0002360](#)].
- [12] C.A. Egan and C.H. Lineweaver, *Dark-energy dynamics required to solve the cosmic coincidence*, *Phys. Rev. D* **78** (2008) 083528 [[0712.3099](#)].
- [13] C. Wetterich, *An asymptotically vanishing time-dependent cosmological “constant”.*, *Astron. Astrophys.* **301** (1995) 321 [[hep-th/9408025](#)].
- [14] G.R. Farrar and P.J.E. Peebles, *Interacting Dark Matter and Dark Energy*, *Astrophys. J.* **604** (2004) 1 [[astro-ph/0307316](#)].
- [15] L. Amendola, *Coupled quintessence*, *Phys. Rev. D* **62** (2000) 043511.
- [16] W. Thipaksorn, S. Sapa and K. Karwan, *Coupled dark energy model inspired from general conformal transformation*, *Phys. Rev. D* **105** (2022) 063527.
- [17] V. Pettorino, *Testing modified gravity with planck: The case of coupled dark energy*, *Phys. Rev. D* **88** (2013) 063519.
- [18] Planck Collaboration, P.A.R. Ade, N. Aghanim, M. Arnaud, M. Ashdown, J. Aumont et al., *Planck 2015 results. XIV. Dark energy and modified gravity*, *Astron. Astrophys.* **594** (2016) A14 [[1502.01590](#)].
- [19] L. Amendola, *Linear and nonlinear perturbations in dark energy models*, *Phys. Rev. D* **69** (2004) 103524 [[astro-ph/0311175](#)].
- [20] L. Amendola, M. Quartin, S. Tsujikawa and I. Waga, *Challenges for scaling cosmologies*, *Phys. Rev. D* **74** (2006) 023525 [[astro-ph/0605488](#)].
- [21] C. Heymans, L. Van Waerbeke, L. Miller, T. Erben, H. Hildebrandt, H. Hoekstra et al., *CFHTLenS: the Canada-France-Hawaii Telescope Lensing Survey*, *Mon. Not. R. Astron. Soc.* **427** (2012) 146 [[1210.0032](#)].
- [22] H. Hildebrandt, M. Viola, C. Heymans, S. Joudaki, K. Kuijken, C. Blake et al., *KiDS-450: cosmological parameter constraints from tomographic weak gravitational lensing*, *Mon. Not. R. Astron. Soc.* **465** (2017) 1454 [[1606.05338](#)].
- [23] Planck Collaboration, P.A.R. Ade, N. Aghanim, M. Arnaud, M. Ashdown, J. Aumont et al., *Planck 2015 results. XIII. Cosmological parameters*, *Astron. Astrophys.* **594** (2016) A13 [[1502.01589](#)].
- [24] A.G. Riess, S. Casertano, W. Yuan, L.M. Macri and D. Scolnic, *Large Magellanic Cloud Cepheid Standards Provide a 1% Foundation for the Determination of the Hubble Constant and Stronger Evidence for Physics beyond  $\Lambda$ CDM*, *Astrophys. J.* **876** (2019) 85 [[1903.07603](#)].
- [25] A. Pourtsidou, C. Skordis and E.J. Copeland, *Models of dark matter coupled to dark energy*, *Phys. Rev. D* **88** (2013) 083505.
- [26] C.G. Boehmer, N. Tamanini and M. Wright, *Interacting quintessence from a variational approach Part I: algebraic couplings*, *Phys. Rev. D* **91** (2015) 123002 [[1501.06540](#)].

- [27] L. Amendola and S. Tsujikawa, *Scaling solutions and weak gravity in dark energy with energy and momentum couplings*, *JCAP* **2020** (2020) 020 [2003.02686].
- [28] M.S. Linton, R. Crittenden and A. Pourtsidou, *Momentum transfer models of interacting dark energy*, *Journal of Cosmology and Astroparticle Physics* **2022** (2022) 075.
- [29] V. Ghirardini, E. Bulbul, E. Artis, N. Clerc, C. Garrel, S. Grandis et al., *The SRG/eROSITA all-sky survey: Cosmology constraints from cluster abundances in the western Galactic hemisphere*, *Astron. Astrophys.* **689** (2024) A298 [2402.08458].
- [30] E. Artis, E. Bulbul, S. Grandis, V. Ghirardini, N. Clerc, R. Seppi et al., *The SRG/eROSITA All-Sky Survey: Constraints on the structure growth from cluster number counts*, *Astron. Astrophys.* **696** (2025) A5 [2410.09499].
- [31] M. Manera and D.F. Mota, *Cluster number counts dependence on dark energy inhomogeneities and coupling to dark matter*, *Mon. Not. R. Astron. Soc.* **371** (2006) 1373 [astro-ph/0504519].
- [32] S. Sapa, K. Karwan and D.F. Mota, *Spherical collapse and cluster number counts in dark energy models disformally coupled to dark matter*, *Phys. Rev. D* **98** (2018) 023528 [1803.02299].
- [33] S.W. Allen, A.E. Evrard and A.B. Mantz, *Cosmological Parameters from Observations of Galaxy Clusters*, *Ann. Rev. Astron. Astrophys.* **49** (2011) 409 [1103.4829].
- [34] S.W. Allen, R.W. Schmidt, A.C. Fabian and H. Ebeling, *Cosmological constraints from the local X-ray luminosity function of the most X-ray-luminous galaxy clusters*, *Mon. Not. R. Astron. Soc.* **342** (2003) 287 [astro-ph/0208394].
- [35] N.A. Bahcall and X. Fan, *The Most Massive Distant Clusters: Determining  $\Omega$  and  $\sigma_8$* , *Astrophys. J.* **504** (1998) 1 [astro-ph/9803277].
- [36] T. Chantavat, C. Gordon and J. Silk, *Probing the primordial power spectrum with cluster number counts*, *Phys. Rev. D* **79** (2009) 083508 [0811.4371].
- [37] T. Chantavat, C. Gordon and J. Silk, *Large scale structure forecast constraints on particle production during inflation*, *Phys. Rev. D* **83** (2011) 103501 [1009.5858].
- [38] L.R. Abramo, R.C. Batista, L. Liberato and R. Rosenfeld, *Structure formation in the presence of dark energy perturbations*, *JCAP* **2007** (2007) 012 [0707.2882].
- [39] C. Horellou and J. Berge, *Dark energy and the evolution of spherical overdensities*, *Mon. Not. R. Astron. Soc.* **360** (2005) 1393 [astro-ph/0504465].
- [40] N.C. Devi, T.R. Choudhury and A.A. Sen, *Constraining thawing dark energy using galaxy cluster number counts*, *Mon. Not. R. Astron. Soc.* **432** (2013) 1513 [1112.0728].
- [41] B.F. Schutz and R. Sorkin, *Variational aspects of relativistic field theories, with application to perfect fluids.*, *Annals of Physics* **107** (1977) 1.
- [42] W.H. Press and P. Schechter, *Formation of Galaxies and Clusters of Galaxies by Self-Similar Gravitational Condensation*, *Astrophys. J.* **187** (1974) 425.
- [43] R.K. Sheth and G. Tormen, *Large-scale bias and the peak background split*, *Mon. Not. R. Astron. Soc.* **308** (1999) 119 [astro-ph/9901122].
- [44] D.S. Reed, R. Bower, C.S. Frenk, A. Jenkins and T. Theuns, *The halo mass function from the dark ages through the present day*, *Mon. Not. R. Astron. Soc.* **374** (2007) 2 [astro-ph/0607150].
- [45] E. Bulbul, A. Liu, M. Kluge, X. Zhang, J.S. Sanders, Y.E. Bahar et al., *The SRG/eROSITA All-Sky Survey. The first catalog of galaxy clusters and groups in the Western Galactic Hemisphere*, *Astron. Astrophys.* **685** (2024) A106 [2402.08452].
- [46] W. Hu and A.V. Kravtsov, *Sample Variance Considerations for Cluster Surveys*, *Astrophys. J.* **584** (2003) 702 [astro-ph/0203169].

- [47] P. Catelan, F. Lucchin, S. Matarrese and C. Porciani, *The bias field of dark matter haloes*, *Mon. Not. R. Astron. Soc.* **297** (1998) 692 [[astro-ph/9708067](#)].
- [48] R.K. Sheth, H.J. Mo and G. Tormen, *Ellipsoidal collapse and an improved model for the number and spatial distribution of dark matter haloes*, *Mon. Not. R. Astron. Soc.* **323** (2001) 1 [[astro-ph/9907024](#)].
- [49] A. Fumagalli, A. Saro, S. Borgani, T. Castro, M. Costanzi, P. Monaco et al., *Euclid : Effects of sample covariance on the number counts of galaxy clusters*, *Astron. Astrophys.* **652** (2021) A21 [[2102.08914](#)].
- [50] M. Costanzi, E. Rozo, M. Simet, Y. Zhang, A.E. Evrard, A. Mantz et al., *Methods for cluster cosmology and application to the SDSS in preparation for DES Year 1 release*, *Mon. Not. R. Astron. Soc.* **488** (2019) 4779 [[1810.09456](#)].
- [51] M. Abramowitz and I.A. Stegun, *Handbook of Mathematical Functions*, Dover (1972).